Research Square

Preprints are preliminary reports that have not undergone peer review.
They should not be considered conclusive, used to inform clinical practice,
or referenced by the media as validated information.

Divergent Bandgap Responses in Cu- and Zn-Doped NiTiO 3 Nanoparticle

Sangamitha V
SRM Institute of Science and Technology
Logamithrai D
SRM Institute of Science and Technology
Debabrata Sarkar
debabras@srmist.edu.in

SRM Institute of Science and Technology

Research Article

Keywords: NiTiO3, Electronic configuration, visible-light photocatalysts, Cu doping, Zn doping, Bandgap engineering

Posted Date: August 11th, 2026

DOI: https://doi.org/10.21203/rs.3.rs-10453466/v1

License: This work is licensed under a Creative Commons Attribution 4.0 International License.
Read Full License

Additional Declarations: No competing interests reported.

Divergent Bandgap Responses in Cu- and Zn-Doped $NiTiO_3$ Nanoparticle

*Sangamitha V, Logamithrai D, Debabrata Sarkar**

Applied Nanophysics Laboratory, Department of Physics and Nanotechnology, SRM Institute of Science and Technology, Kattankulathur - 603203, Tamil Nadu, India.

*Corresponding author: Email – debabras@srmist.edu.in, deboo_phy@yahoo.com

ABSTRACT:

Nickel titanate ($NiTiO_3$) nanoparticles doped with Cu and Zn were successfully synthesized via a modified Pechini sol-gel method to investigate the influence of dopant electronic configuration on the structural, optical, and photocatalytic properties of $NiTiO_3$. The synthesized materials were systematically characterized using X-ray diffraction (XRD), Raman spectroscopy, scanning electron microscopy (SEM), high-resolution transmission electron microscopy (HR-TEM), and UV–Vis diffuse reflectance spectroscopy. Structural analyses confirmed the formation of phase-pure rhombohedral $NiTiO_3$ with nanocrystalline morphology, while the result revealed slight lattice expansion resulting from the substitution of larger Cu^{2+} and Zn^{2+} ions at the Ni site without altering the host crystal structure. Optical investigations demonstrated distinctly different electronic responses for the two dopants. Cu doping produced a pronounced redshift in the absorption edge and reduced the optical band gap from approximately 2.1 to 1.75 eV, whereas Zn doping caused negligible changes in the band gap. This contrasting behavior is attributed to the partially filled Cu^{2+} ($3d^9$) electronic configuration, which introduces Cu 3d-derived impurity states and enhances O 2p-Cu 3d

hybridization near the valence band, while the fully filled Zn^{2+} ($3d^{10}$) configuration does not significantly modify the electronic structure. The improved electronic structure of Cu-doped $NiTiO_3$ resulted in superior visible-light photocatalytic performance toward cationic thiazine dye degradation. These findings demonstrate that dopant electronic configuration plays a decisive role in tailoring the band structure and photocatalytic activity of $NiTiO_3$, providing an effective strategy for designing high-performance visible-light-responsive oxide photocatalysts.

KEYWORDS: $NiTiO_3$; Electronic configuration; visible-light photocatalysts; Cu doping; Zn doping; Bandgap engineering.

1. INTRODUCTION

Over the last several decades, mixed and multi-component metal oxides have emerged as a versatile class of functional materials for photocatalytic and photoelectrochemical applications. Their compositional flexibility enables precise tuning of band structure, defect chemistry, and surface energetics, which are critical for optimizing light absorption and charge carrier dynamics [1–3].

Such systems have been extensively investigated for solar-driven water splitting, degradation of persistent organic pollutants, selective CO_2 reduction, and various electrocatalytic processes [4–6].In addition, their stability, cost-effectiveness, and environmental compatibility make them attractive for practical implementations such as indoor air purification, self-cleaning coatings, and odor removal technologies[7–9]. The cooperative interactions between different metal cations often promote improved charge separation and enhanced redox reactivity, thereby outperforming single-component oxides in many catalytic scenarios [7,10–12].

Metal oxide nanoparticles have garnered significant research interest due to their broad applications across energy, environmental remediation, medical diagnostics, catalysis, and optoelectronics. Their unique electrical, optical, chemical, and magnetic properties-arising from nanoscale size and controlled morphology-make them highly versatile functional materials [7–12]. Consequently, tailoring their size, shape, and structure continues to be a key focus in advancing next-generation technologies [13,14]. Perovskite-type oxides, with the general formula ABO_3, have emerged as promising candidates due to their structural flexibility, chemical stability, and tunable electronic properties [14–16].

The perovskite structure allows for extensive substitution at both the A-site and B-site, enabling precise control over the bandgap, carrier mobility, and band alignment. Nickel titanate ($NiTiO_3$) is a perovskite-type oxide that has attracted attention for its potential in photocatalyst, pigment, catalyst and gas sensor applications. $NiTiO_3$ adopts an ilmenite-type structure, which is a double transition metal oxide [17–19].

The structure consists of a hexagonal close-packed array of oxygen anions, containing Ni and Ti with an octahedral coordination [MO_6] within which nickel (Ni^{2+}) and titanium (Ti^{4+}) cations occupy two-thirds of the available octahedral sites in an ordered, alternating fashion along the crystallographic c-axis. $NiTiO_3$ is an n-type semiconductor with a low band gap of around 2.18 eV to 3 eV [20,21].

The low band gap makes $NiTiO_3$ suitable for electrons excitation to the conduction band using visible light. However, $NiTiO_3$ has been limited by its poor quantum efficiency and fast recombination rate when applied as an individual phase photocatalyst.[22–25] Its band structure can be engineered through doping and compositional modifications to enhance visible-light absorption and improve charge separation. Incorporating transition metal dopants such as Mn, Cr, Cu, Zn, and Cd can introduce new energy levels, reduce the charge carrier recombination

rates.[26–30] and morphology of the resulting material, all of which impact photocatalytic performance.So far, various wet-chemical and solid-state approaches have been developed to synthesize $NiTiO_3$ nanoparticles, including polymer pyrolysis, sol-gel processing, dip coating, stearic-acid gel methods, auto-combustion routes, co-precipitation, and conventional solid-state synthesis[31–35].

In this research, $NiTiO_3$ nanoparticles were synthesized using a modified Pechini sol-gel method, which enables molecular-level mixing of precursors and precise control over stoichiometry. The morphological, optical, and structural properties of doped $NiTiO_3$ were systematically investigated. Specifically, we examined the effect of incorporating nearly filled (Cu^{2+}) and fully filled (Zn^{2+}) 3d-band elements at the Ni site of the $NiTiO_3$ lattice. Cu and Zn dopants were selected because their effective ionic radii (Ni^{2+}: 0.69 Å, Cu^{2+}: 0.73 Å, Zn^{2+}: 0.74 Å) closely match that of Ni^{2+}, allowing substitution without significant lattice distortion.

2. EXPERIMENTAL TECHNIQUES

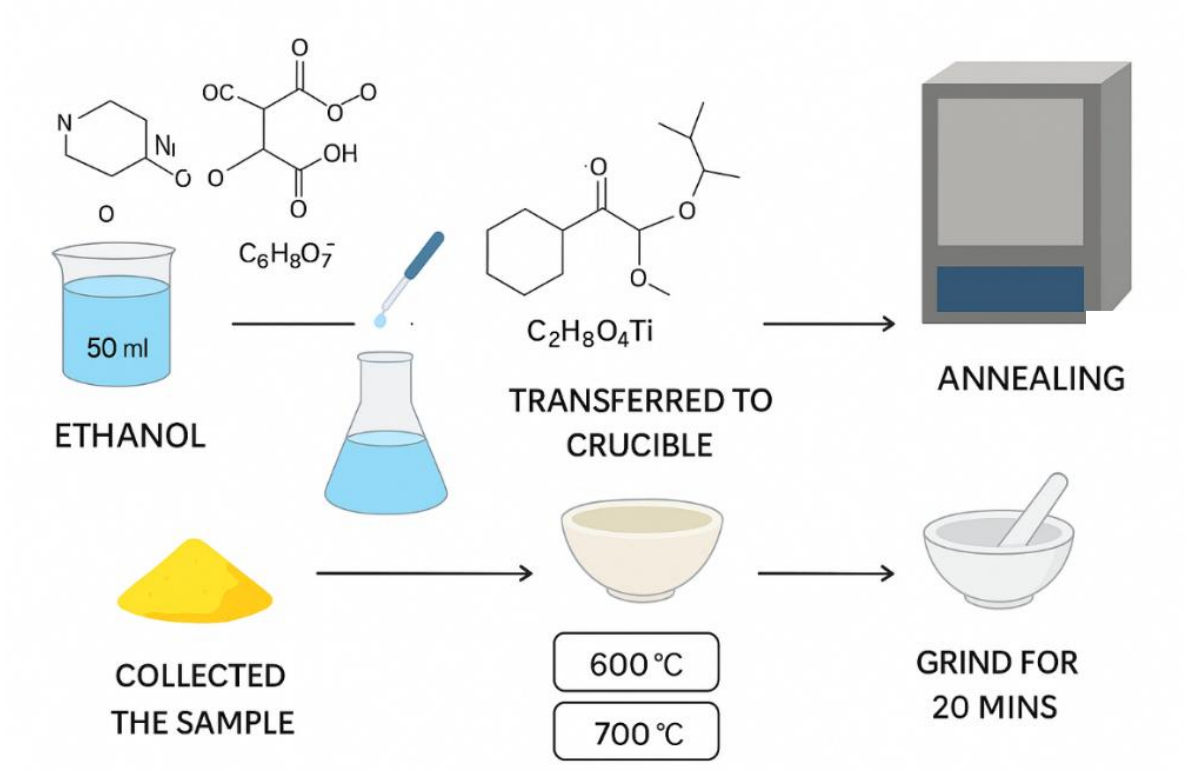
2.1. Materials

Citric acid ($C_6H_8O_7$), ethanol (C_2H_5OH), nickel acetate tetrahydrate ($Ni(CH_3COO)_2{\cdot}4H^2O$), and titanium isopropoxide ($Ti[OCH(CH_3)_2]_4$) were used as starting materials for the synthesis Of $NiTiO_3$ nanoparticles. Copper acetate ($Cu(CH_3COO)_2$) and zinc acetate ($Zn(CH_3COO)_2$) Were used as dopant precursors for the preparation of Cu- and Zn-doped samples. All Chemicals were of analytical grade and used as received without further purification. Calcination was carried out in ambient air.

2.2 Synthesis of $NiTiO_3$ Nanoparticles

$NiTiO_3$ nanoparticles were synthesized using a sol-gel method. First, 5.76 g of citric acid was dissolved in 50 mL of ethanol and magnetically stirred for 15 min. Subsequently, 1.178 g of nickel acetate tetrahydrate was added, and the solution was stirred for an additional 30 min to obtain a homogeneous mixture. 1.48 µl of Titanium isopropoxide was then introduced dropwise into the solution, resulting in a transparent light-green sol, which was stirred for 1 h. The sol was transferred to an oven at 70 °C for 2 days to facilitate gel formation. The resulting gel was finally calcined in air at 650 °C for 5 h to obtain $NiTiO_3$ nanoparticles.

For the Cu- and Zn-doped samples, the required amount of copper acetate or zinc acetate (three different molar ratio; 0.005, 0.0075 and 0.01 M) was added to the mixture immediately after the addition of titanium isopropoxide, followed by continuous stirring to ensure uniform incorporation of the dopant ions.



Scheme: 1: Schematic of $NiTiO_3$ nanoparticle synthesis via sol–gel method and annealing.

2. 3. Characterization

The crystalline structure and phase constitution of the synthesized samples were analyzed using a D8 Advance X-ray Diffractometer (Bruker AXS, USA) equipped with Cu Kα radiation (λ = 1.5418 Å). Optical absorbance measurements were performed using an Agilent Cary 5000 UV-Vis spectrophotometer in the wavelength range of 200-800 nm. The surface morphology and elemental composition were examined using High-Resolution Scanning Electron Microscopy (HRSEM) on a Thermo Scientific Apreo S microscope. The microstructure, particle morphology, crystallinity, and lattice fringes were investigated using High-Resolution Transmission Electron Microscopy (HRTEM) (JEOL, Japan). The vibrational bonding characteristics and structural defects were analysed using a HORIBA LabRAM HR Evolution Raman spectrometer.

2. 4. Photocatalytic Degradation of Pollutants.

The photocatalytic activity of the synthesized samples was evaluated by degrading Rhodamine B model organic pollutant under Visible light irradiation. A predetermined concentration of the pollutant was prepared in deionized (DI) water in a quartz beaker and stirred for 15 min to ensure complete dissolution. Subsequently, 40 mg of the photocatalyst was dispersed into the solution, and the suspension was magnetically stirred in the dark for 30 min to establish adsorption-desorption equilibrium. At regular time intervals, aliquots were withdrawn, and the residual pollutant concentration was determined using a UV-Vis spectrophotometer.

3. RESULTS AND DISCUSSION

3.1. Nanoparticle formation mechanism

$NiTiO_3$ nanoparticles were synthesized via a modified sol-gel method, which enables molecular-level mixing of metal precursors and precise control over stoichiometry and phase purity. Initially, nickel acetate was dissolved in ethanol, a polar protic solvent, and stirred vigorously for 15 minutes to ensure complete dissociation of Ni^{2+} ions and formation of a homogeneous precursor solution. Citric acid (H_3Cit) was then introduced as a chelating agent, facilitating the formation of stable metal-citrate complexes through coordination bonding, which prevents premature precipitation and ensures uniform distribution of cations.

Subsequently, titanium butoxide, serving as the titanium source, was added dropwise under continuous stirring. The slow addition of titanium isopropoxide was critical to control the hydrolysis and condensation reactions characteristic of metal alkoxides [36] thereby promoting the formation of a stable sol. The system was stirred for an additional hour, allowing the sol to transition into a gel via polycondensation and esterification reactions, resulting in a three-dimensional polymeric network (Ni-Ti-O) that immobilizes the metal ions within an organic matrix. [37,38].The gel was then subjected to drying at 70 °C for 48 hours, during which solvent evaporation and further condensation occurred, yielding a xerogel. The calcination process induces thermal decomposition of organic residues, solid-state diffusion, and crystallization, leading to the formation of the rhombohedral $NiTiO_3$ phase.

Step 1: Chelation (Solution Phase)

Nickel acetate ($Ni(CH_3COO)_2$) and Titanium (IV) Isopropoxide ($Ti(OiPr)_4$) are dissolved in a solvent (ethanol or water), with citric acid (H_3Cit) added as a chelating agent.

$$Ni(aq)2 + H_3Cit(aq) \rightarrow [Ni\ (Cit)]\ (aq) + 3H(aq) + Ni\ (CH_3COO)2_{(aq)} + H_3Cit_{(aq)} \rightarrow [Ni\ (Cit)]^-{}_{(aq)} + 2CH_3COOH_{(aq)} + H^+{}_{(aq)}$$

Citric acid coordinates with $Ni^{2+,}$ forming a stable nickel-citrate complex and preventing premature precipitation. This ensures homogeneous mixing and controls the hydrolysis/condensation rates of the metal precursors.

Step 2: Hydrolysis and Condensation (Sol-Gel Transition)

Hydrolysis of titanium precursor:

$$Ti\ (OiPr)_{4(aq)} + 4H2O_{(l)} \rightarrow Ti\ (OH)_{4(aq)} + 4iprOH_{(aq)}$$

Condensation (polymerization):

$$Ti\ (OH)_{4(aq)} \rightarrow (Ti–O–Ti)_{(gel)} + 2H_2O_{(l)}$$

The solution transitions from a clear sol (liquid) to a viscoelastic gel (solid network) as condensation proceeds. [39,40]

Step 3: Gelation, Drying, and Calcination (Solid-State Transformation)

The gel is aged, allowing the network to strengthen and solvent to be removed from the pores. The gel is dried (typically at 70 °C) to remove residual solvents and water, resulting in a xerogel (solid, amorphous phase).

The dried gel is heated in air at 650°C. During this process, organic residues are combusted, and the amorphous network crystallizes to form the perovskite phase of nickel titanate.

Overall calcination reaction:

$$\text{calcination}\ [Ni\ (Cit)]_{(gel)} + Ti\ (OH)_{4(gel)} \xrightarrow{650^{o}C} NiTiO_3 + \text{gaseous byproducts } (CO_2, H_2O, \text{etc.})$$

$$\text{Amorphous xerogel} \xrightarrow{\text{calcination}} \text{crystalline } NiTiO_3 \text{ (solid) + gases } (CO_2, H_2O, \text{etc.})$$

After chelation and hydrolysis, the nickel-citrate complex and titanium hydroxide/polymer species condense to form a mixed Ni-Ti-O gel network:

$$[Ni\ (Cit)]_{(aq)} + Ti\ (OH)_{4(aq)} \xrightarrow{condensation} Ni–O–Ti–O–Ti–O–(gel)_{(s)} + Cit^{3-}_{(aq)} + H_2O_{(l)}$$

$$Ni^{2+}_{(aq)} + Ti\ (OH)_{4(aq)} \xrightarrow{condensation} Ni–O–Ti–O–Ti–O–(gel)_{(s)} + H_2O_{(l)}$$

$$Ni^{2+} + Ti–O–Ti \rightarrow Ni–Ti–O(gel)$$

The nickel and titanium species condense to form a three-dimensional Ni–Ti–O gel network[41]. Water is released as a byproduct of the condensation/polymerization process.

Step 4: Gel Combustion and Calcination

During calcination, the amorphous Ni – Ti – O gel undergoes combustion and crystallization to form nickel titanate:

$$Ni–Ti–O\ (gel) \xrightarrow{650\ °C,\ air} NiTiO_3 + \text{gaseous byproducts}$$

(showing organic removal):

$$Ni–Ti–O(gel) \xrightarrow{650^{0}C,\ air} NiTiO_3 + CO_2 + H_2O\ (g) + \text{other gases}$$

$$Ni–Ti–O(gel) \xrightarrow{650^{0}C,\ air} \text{calcination} \rightarrow NiTiO_3$$

3.2. Morphological Analysis

3.2.1. Scanning Electron Microscopy (SEM) study

HR-SEM was utilized to examine the surface morphology and particle distribution of the annealed $NiTiO_3$ nanoparticles. The SEM images revealed that the nanoparticles possess a uniform, well-dispersed morphology with no significant agglomeration, a feature that is characteristic of high-quality nickel titanate synthesized via sol–gel methods. The uniformity

in particle shape and distribution was consistent across samples annealed at temperature (650°C), indicating that the thermal treatment did not adversely affect the morphology. Image analysis using Gatan Digital Micrograph software estimated the average particle size to be approximately 32 nm, which is advantageous for photocatalytic applications due to the increased surface area available for reaction.

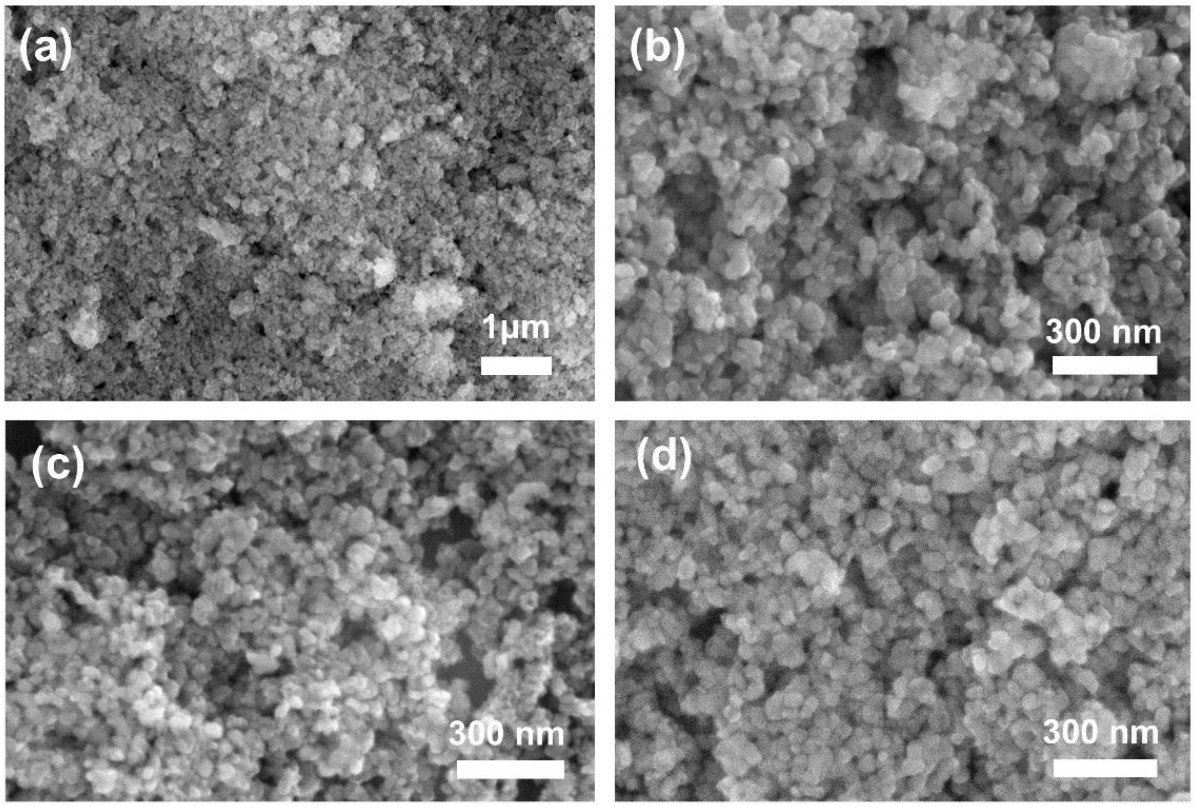


Figure 1. FE-SEM micrographs of $NiTiO_3$ nanoparticles showing (a) undoped $NiTiO_3$ at low magnification, (b) undoped $NiTiO_3$ at high magnification, (c) Cu-doped $NiTiO_3$, and (d) Zn-doped $NiTiO_3$.

3.2.2. High-Resolution Transmission Electron Microscopy (HR-TEM)

High-resolution transmission electron microscopy (HR-TEM) provided further insight into the internal structure and crystallinity of $NiTiO_3$ nanoparticles. Micrographs at 5 nm, 10 nm, and

50 nm enlargement essentially show distinct, particle-like nanocrystals with regular, periodic lattice patterning. The appearance of clear lattice fringes and distinctly resolved grain boundaries is direct evidence for the high crystallinity at the nanoscale. The structural properties of crystalline materials are crucial for efficient charge carrier transport. That is, a high level of crystallinity allows minimizing the density of structural defects and grain boundary traps that can recombine photogenerated electrons and holes[42].

The nanocrystalline domains that have uniform morphology and ordered atomic planes observed in synthesized $NiTiO_3$ create a suitable pathway to prepare charge separation and migration that reduces the electron–hole recombination and enhances the overall photocatalytic efficiency[43,44]. The high-resolution TEM (HRTEM) image (Figure 2c) clearly displays well-resolved lattice fringes, indicating the crystalline nature of the sample. The selected crystalline region (red marked area) was processed in the frequency domain using fast Fourier transform (FFT) followed by inverse fast Fourier transform (IFFT) filtering to enhance the lattice information. The reconstructed image shows distinct lattice fringes corresponding to the crystallographic planes. The line intensity profile taken across the lattice fringes reveals an interplanar spacing of ~0.26 nm, which can be indexed to the (104) plane of $NiTiO_3$, confirming the successful formation of crystalline $NiTiO_3$ nanoparticles.

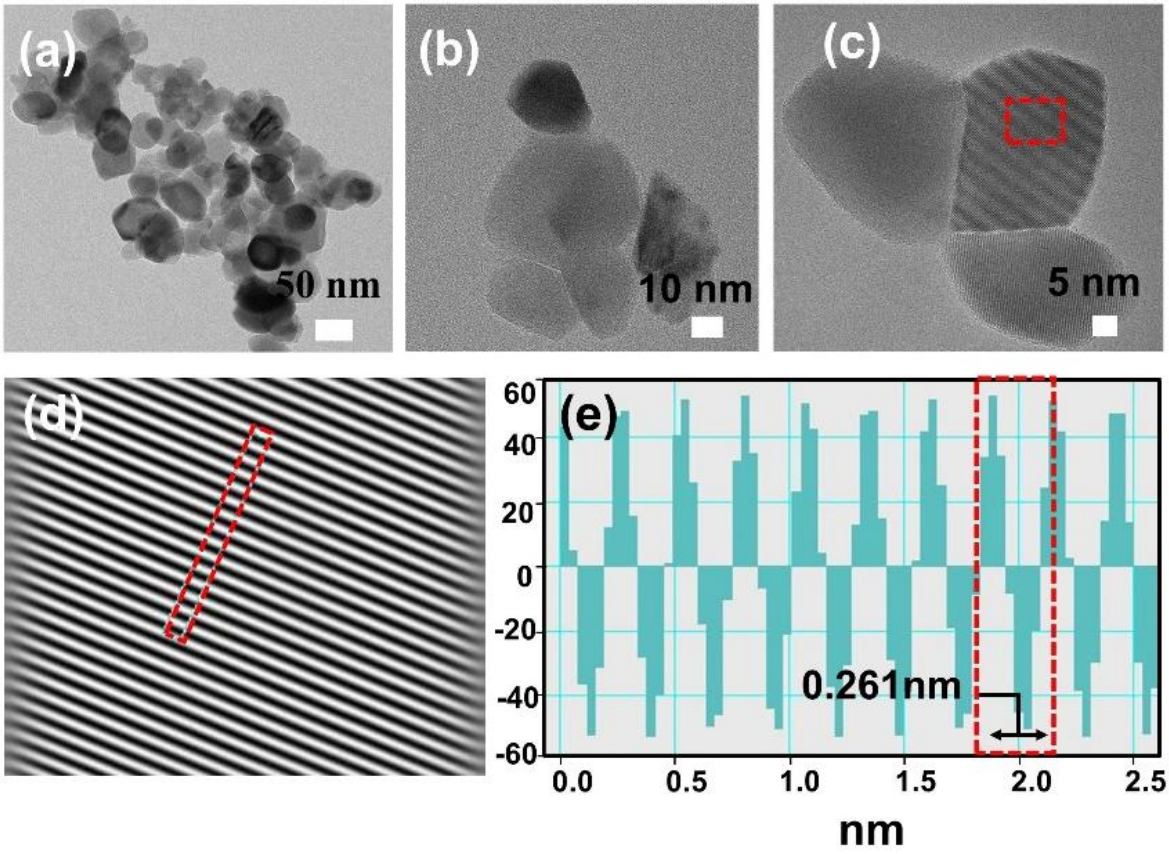


Figure 2. HR-TEM images of $NiTiO_3$ nanoparticles recorded at different magnifications (a) Agglomerated nanoparticles with a 50 nm scale bar, (b) Individual nanocrystals with a 10 nm scale bar, and (c) Highly magnified nanoparticles with a 5 nm scale bar, (d) The lattice-resolved HRTEM image and (e) corresponding line profile analysis confirm the crystalline nature of the nanoparticles with an interplanar spacing of 0.261 nm.

3.2.3. Phase Identification and Crystallite Size: X-ray Diffraction (XRD)

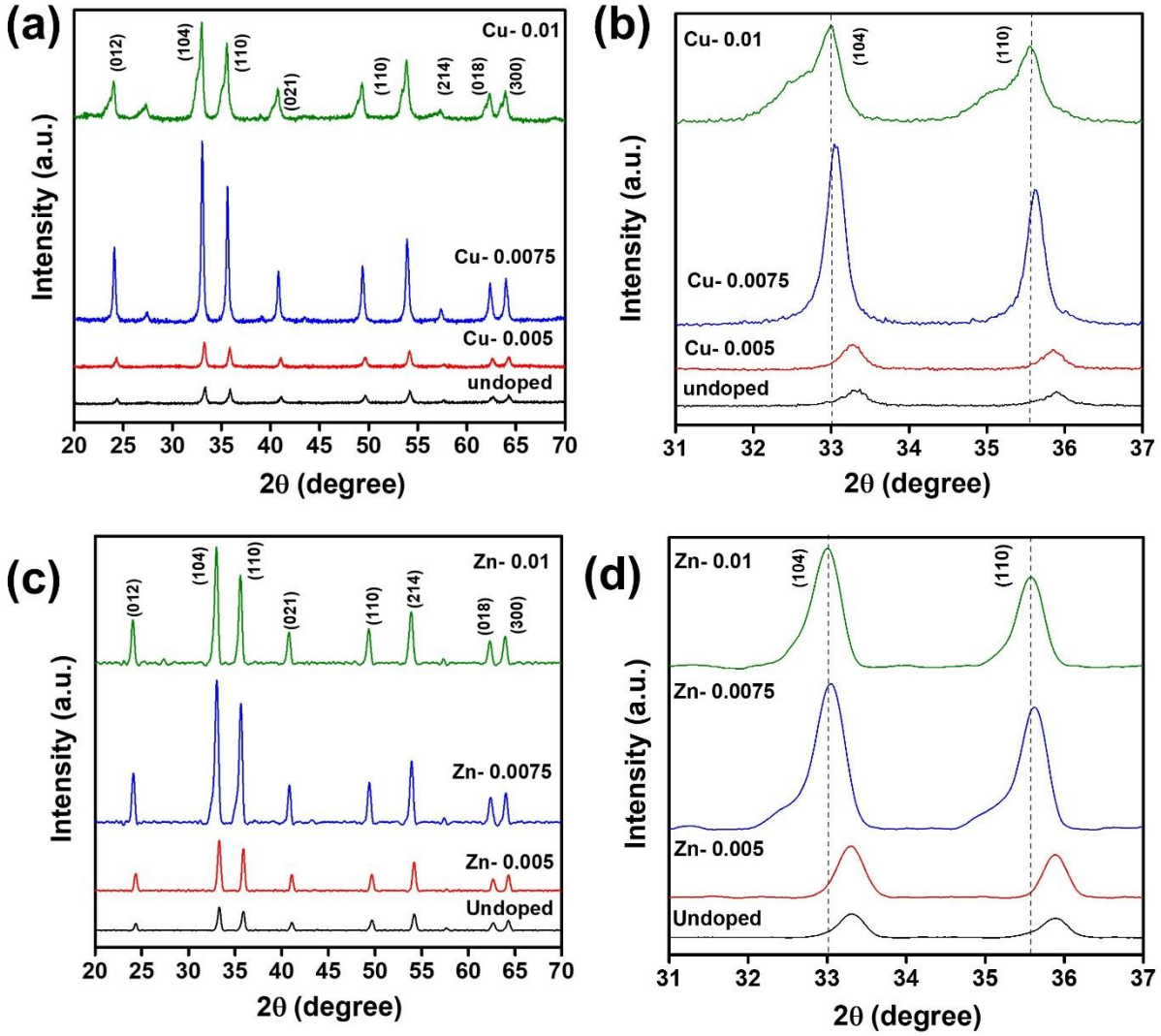


Figure 3. XRD patterns of undoped and Cu-/Zn-doped $NiTiO_3$ nanoparticles, where (a) Cu-doped samples, (b) enlarged (104) and (110) peaks of Cu-doped samples, (c) Zn-doped samples, and (d) enlarged (104) and (110) peaks of Zn-doped samples. The diffraction peak shifts indicate lattice distortion due to Cu and Zn incorporation into the $NiTiO_3$ structure.

The crystal phase and average crystallite size of the $NiTiO_3$ nanoparticles were further investigated using X-ray diffraction (XRD) analysis. XRD patterns for undoped $NiTiO_3$ and nanoparticle doped with increasing concentrations of Cu (0.005, 0.0075, and 0.01 M) over a broad 2θ range (20-70°) are shown in Figure 3. All samples exhibit characteristic peaks indexed to the rhombohedral $NiTiO_3$ phase (JCPDS # 33-0960), with no evidence of secondary phases or impurities, indicating high phase purity and successful synthesis, including (012), (104),

(110), (021), (214), (018), and (200). The absence of extra peaks confirms that no impurity oxides are present, indicating that the Cu and Zn dopants are successfully incorporated into the $NiTiO_3$ lattice without disrupting the host structure. The relative intensities and sharpness of the peaks suggest good crystallinity across all samples.

A magnified view of the (104) and (110) reflections for the same set of samples (Figure 3c,d) reveals a systematic shift of these peaks toward lower 2θ values as the Cu dopant concentration increases. This shift, highlighted by dashed vertical lines, indicates an expansion of the unit cell, which is consistent with the substitution of Ni^{2+} by the slightly larger Cu^{2+} ions. The peak shift is more pronounced at higher doping levels, confirming that the lattice parameters are sensitive to the amount of Cu incorporated. Similarly, Figure 3c, presents the XRD patterns for undoped $NiTiO_3$ and samples doped with Zn at 0.005, 0.0075, and 0.01 M, again over a broad 2θ range. The patterns are nearly identical to those of the Cu-doped series, with all major peaks matching the standard $NiTiO_3$ phase and no evidence of secondary phases. This demonstrates that Zn, like Cu, is effectively incorporated into the $NiTiO_3$ lattice without forming separate ZnO or other impurity phases. The consistent peak positions and intensities across the series further confirm the structural integrity and phase purity of the samples. From the peak (104) and (110) peaks for the Zn-doped and undoped samples (Figure 3d) shows a clear shift of these peaks toward lower 2θ values with increasing Zn content. The shift, again marked by dashed lines, is attributed to the substitution of Ni^{2+} (ionic radius ≈ 0.69 Å) with the slightly larger Zn^{2+} ions (≈ 0.74 Å), leading to an increase in the lattice spacing (d-spacing). The systematic nature of the shift with increasing Zn concentration confirms successful doping and lattice expansion. The average crystallite size of the synthesized $NiTiO_3$ nanoparticles was estimated using the Debye–Scherrer equation[45,46],which relates the broadening of X-ray diffraction peaks to the size of coherently diffracting domains. The equation is given by

$$D = \frac{k\lambda}{\beta \cos\theta}$$

where D represents the average crystallite size, K is the shape factor (commonly taken as 0.9 for spherical particles), λ is the wavelength of the X-ray radiation (for copper K-alpha radiation, = 1.5406 \ Å), β is the full width at half maximum of the selected diffraction peak (measured in radians), and θ is the Bragg angle corresponding to that peak. In this study, the (104) diffraction peak, which is the most intense and well-defined in the $NiTiO_3$ X-ray diffraction pattern, was chosen for the calculation. The full width at half maximum was corrected for instrumental broadening to ensure accuracy. The Debye-Scherrer equation assumes that the observed peak broadening is primarily due to the finite size of the crystallites and does not account for other factors such as lattice strain or defects. Therefore, the calculated crystallite size reflects the dimensions of single-crystal domains within the nanoparticles, which may be smaller than the overall particle size observed by electron microscopy. In this work, the application of the Debye-Scherrer equation yielded an average crystallite size of approximately 25.1 nanometres for the $NiTiO_3$ nanoparticles, in agreement with the nanoscale features observed in high-resolution transmission electron microscopy and scanning electron microscopy analyses.

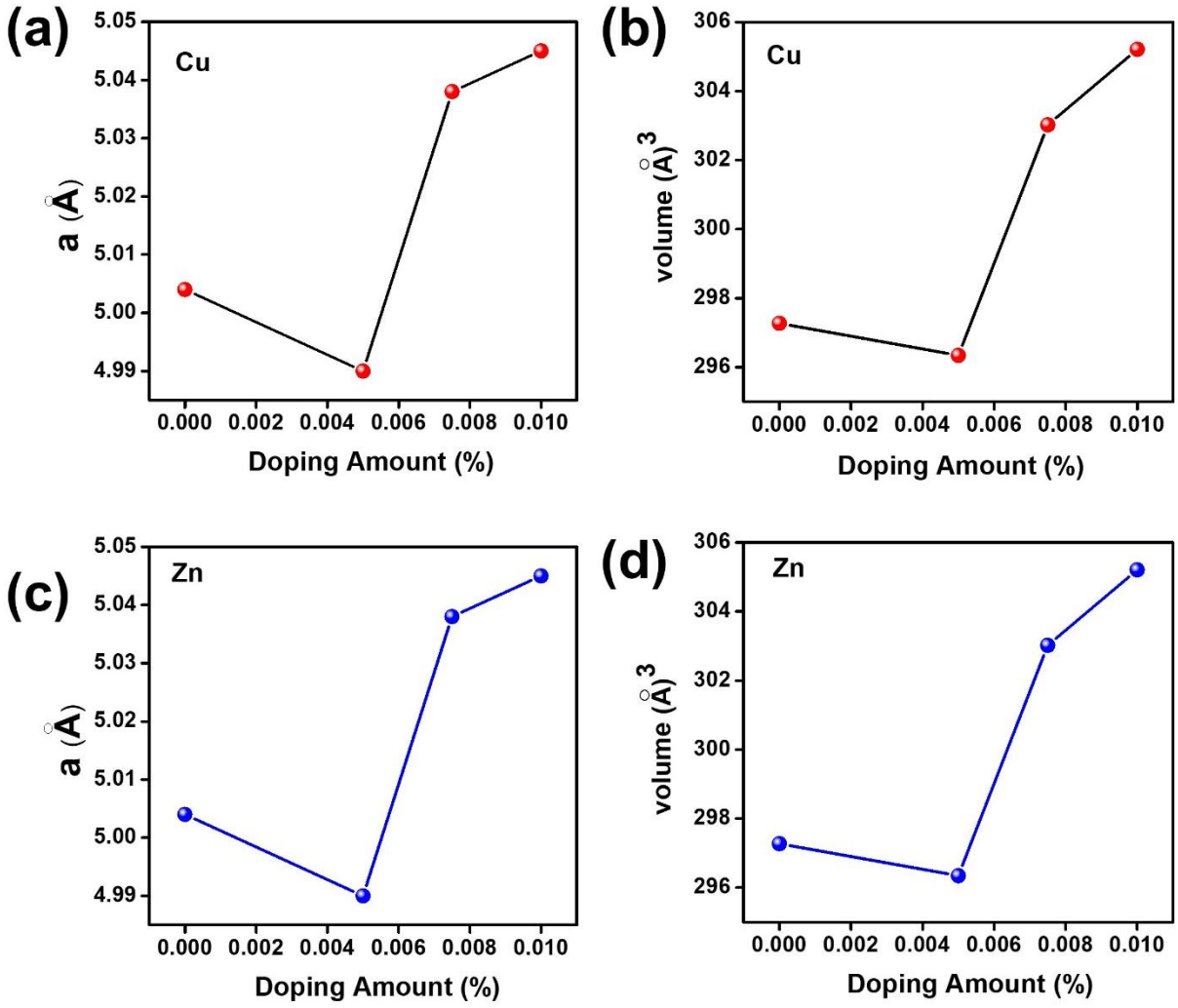


Figure 4. Variation of lattice parameter and unit cell volume for (a, b) Cu-doped samples and (c, d) Zn-doped samples.

At low Cu doping, a slightly decreases, likely due to initial lattice distortion or local strain[47]. As the Cu content increases further, a increases significantly. This is because Cu^{2+} ions (ionic radius ≈ 0.73 Å) are slightly larger than Ni^{2+} (≈ 0.69 Å)[48,49], so substituting more Cu into the Ni site expands the lattice in the a-direction. The c parameter follows a similar trend to a, with a slight initial decrease and then a marked increase at higher Cu concentrations. This reflects the three-dimensional response of the crystal lattice, where the incorporation of larger Cu^{2+} ions results in expansion along both the a- and c-axes. Consequently, the unit cell volume (Fig. 4b,d) increases progressively with increasing Cu content, confirming overall lattice expansion

due to ionic size mismatch. A similar structural trend is observed for Zn-doped $NiTiO_3$. The lattice parameter a initially shows a slight decrease at low Zn concentrations, followed by a notable increase with higher doping levels. This can be attributed to the substitution of Ni^{2+} by larger Zn^{2+} ions (ionic radius ≈ 0.74 Å), which induces lattice expansion. The c parameter also increases with Zn incorporation, consistent with the behavior observed in Cu-doped samples and indicative of isotropic expansion of the unit cell. As a result, the unit cell volume increases systematically with Zn content, confirming that Zn doping, like Cu doping, leads to an overall expansion of the $NiTiO_3$ lattice. This structural evolution is consistent with Vegard's law[50] and supports the successful substitution of larger dopant ions at the Ni site.

3.2.4 Vibrational and Structural Symmetry: Raman Spectroscopy

Raman spectroscopy was employed to probe the vibrational modes and structural symmetry of the $NiTiO_3$ nanoparticles. The Raman spectra displayed ten well-resolved modes, consistent with the rhombohedral phase of $NiTiO_3$ as reported in the literature[51].

The observed peaks are primarily associated with Ti-O stretching and bending vibrations within the octahedral framework of the perovskite structure[52]. Curve fitting of the spectral data improved the resolution of overlapping modes, providing detailed information on local lattice distortions and site symmetry[53].

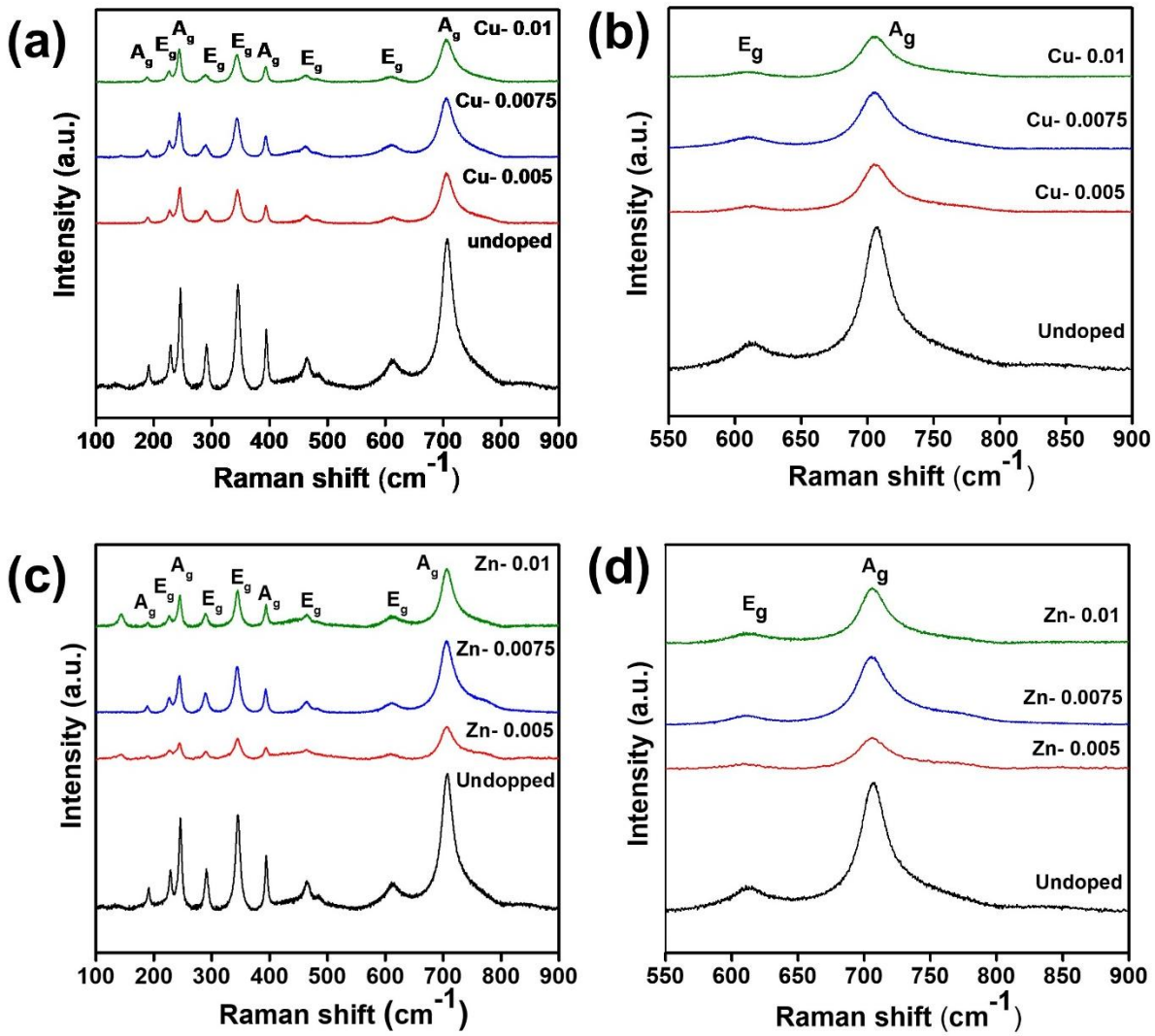


Figure 5. Raman spectra showing the full spectral range for (a) Cu-doped, and the enlarged high-frequency region for (b) Cu-doped samples, Raman spectra showing the full spectral range for (c) Zn-doped samples, and the enlarged high-frequency region for (d) Zn-doped samples.

The Raman spectra of undoped, Zn-doped, and Cu-doped $NiTiO_3$ exhibit well-defined Ag and Eg phonon modes characteristic of the rhombohedral ilmenite structure (space group $R\bar{3}$)[19,54],

confirming the preservation of long-range crystallographic symmetry upon doping. These Raman-active modes originate from zone-centre optical phonons associated predominantly with TiO_6 octahedral vibrations and Ni-O lattice dynamics[54,55]. The negligible variation in

peak positions and relative intensities between undoped and doped samples indicates that the average lattice force constants and overall bonding framework remain largely unaffected by substitution. Furthermore, the absence of additional Raman modes or significant peak splitting suggests that neither Zn nor Cu incorporation induces any symmetry-lowering phase transition or long-range structural distortion.

However, observed in the high-frequency region corresponding to Ti-O stretching modes. In Zn-doped samples, minor shifts in the Ag and Eg modes, accompanied by slight peak broadening, can be attributed to local lattice strain arising from the substitution of Ni^{2+} (≈ 0.69 Å) with larger Zn^{2+} ions (≈ 0.74 Å) [56].This ionic size mismatch perturbs local bond lengths and angles, leading to small variations in force constants and enhanced phonon scattering, as reflected in the increased linewidths. In contrast, Cu doping introduces additional local distortions due to the Jahn-Teller activity of Cu^{2+} (3d configuration, ≈ 0.73 Å), which induces anisotropic deformation of the surrounding oxygen octahedra[48,53]. This results in localized symmetry breaking at the atomic scale, modifying the crystal field environment and slightly altering phonon frequencies, linewidths, and intensities.

3.2.5 Optical Properties: UV–Visible Absorption Spectroscopy

The optical properties of the synthesized $NiTiO_3$ nanoparticles were investigated using ultraviolet-visible (UV-Vis) absorption spectroscopy in the wavelength range of 200 to 800 nm. As shown in Fig.6, the UV-Vis absorption spectrum displays prominent peaks at approximately 326 nm and 443 nm, indicating strong photon absorption and efficient electronic transitions within the $NiTiO_3$ lattice[57,58]. To quantitatively determine the optical band gap, both direct and indirect Tauc plots were constructed. The Tauc relation[5,59,60]

is given by:

$(\alpha hv)^n = A(hv - Eg)$

The above equation is the absorption coefficient; h is Planck's constant, is the frequency of the incident photon, A is a proportionality constant, Eg is the optical band gap energy, n is the exponent that depends on the nature of the electronic transition (n = 2) for direct allowed transitions, (n = 1) for indirect allowed transitions[61].

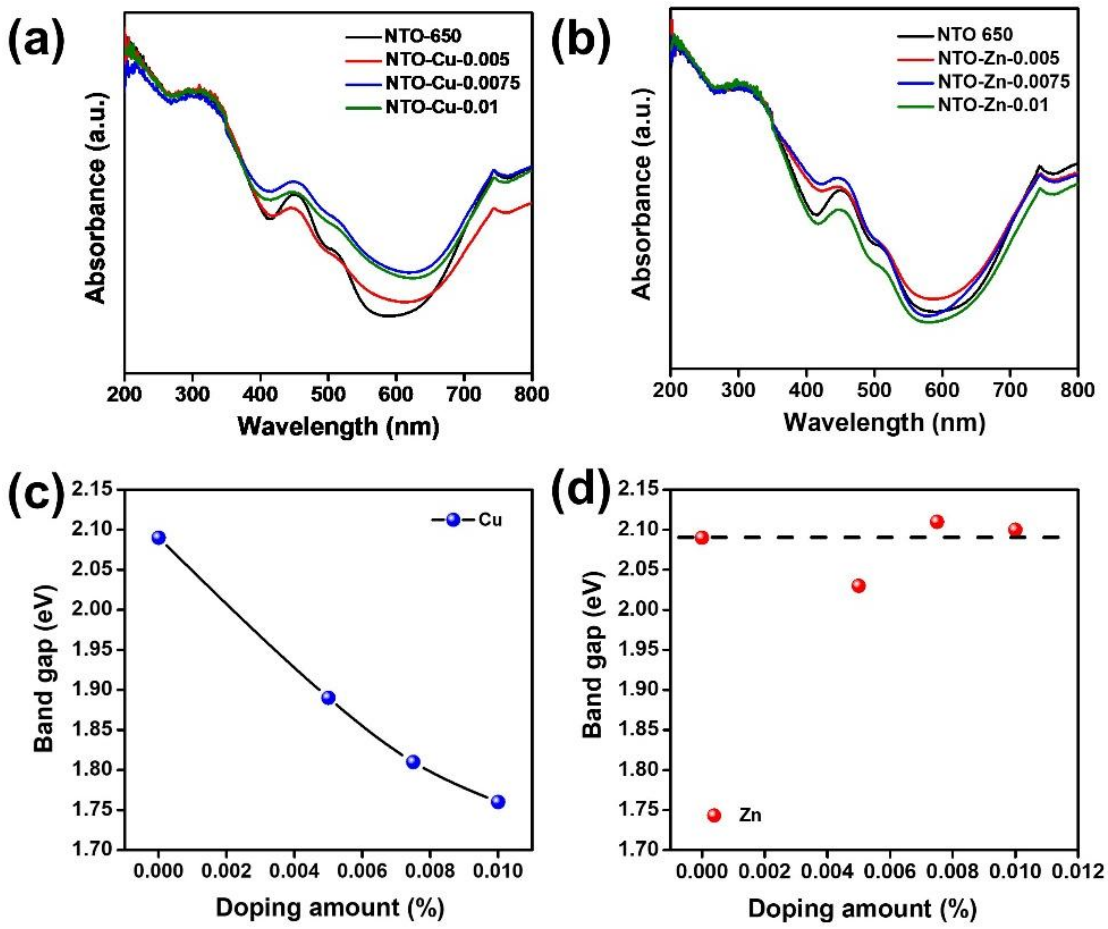


Figure 6. UV-Vis absorbance spectra of (a) Cu-doped $NiTiO_3$ and (b) Zn-doped NTO with varying doping percentages, and the corresponding optical band gap energy (E_g) variation as a function of doping amount for (c) Cu-doped samples and (d) Zn-doped samples, highlighting the pronounced band gap narrowing effect induced by Cu incorporation compared to Zn doping.

Figure 6 presents the UV-Vis absorbance spectra and the corresponding optical band gap (Eg) analysis for undoped and Cu- or Zn-doped $NiTiO_3$ nanoparticles. All samples display strong absorbance in the ultraviolet region, with a pronounced absorption edge extending into the visible range. Zn-doped $NiTiO_3$ samples, the corresponding band gap values fluctuate only slightly around the undoped value (~2.1 eV), indicating that Zn^{2+}, being isoelectronic and similar in size to Ni^{2+}, does not significantly perturb the electronic band structure or introduce new states within the band gap. As a result, the optical properties and light absorption characteristics of Zn-doped $NiTiO_3$ remain relatively stable, with only minor changes in the visible region. For the Cu-ion region, with a pronounced absorption edge extending into the visible range. For the Cu-doped series, increasing the Cu concentration (0.005, 0.0075, and 0.01 M) results in a clear red-shift of the absorption edge, as well as an overall increase in visible-light absorbance. This red-shift indicates a reduction in the optical band gap, which is quantitatively confirmed by the Tauc plot analysis. The band gap decreases systematically from approximately 2.1 eV for undoped $NiTiO_3$ to about 1.75 eV at the highest Cu doping level. The band gap narrowing can be attributed to the introduction of Cu 3d states into the $NiTiO_3$ electronic structure. The substitution of Ni^{2+} by Cu^{2+} ions perturb the local crystal field and introduces additional electronic states near the conduction band minimum or valence band maximum. This results in a reduction of the energy required for electronic transitions. The enhanced visible-light absorption is particularly beneficial for photocatalytic applications, as it allows the material to utilize a larger fraction of the solar spectrum, thereby increasing the generation of photogenerated charge carriers available for redox reactions.

4. PHOTOCATALYTIC DEGRADATION PERFORMANCE

The photocatalytic performance of the synthesized $NiTiO_3$ nanoparticle catalyst was examined through the degradation of methylene blue (MB) under visible-light irradiation. Because

methylene blue is a stable, complex molecule that does not degrade on its own, it is commonly used as a model pollutant in these tests. This renders it an ideal candidate for assessing the efficacy of photocatalysts for water purification. When the catalyst absorbs light, it forms highly reactive species on the surface, which target and decompose the dye compounds. The effectiveness of this process depends on the ability of the catalyst to dissociate the charge carriers (electrons and holes) generated by the light [62], as well as the availability of active sites on the catalyst surface. Before illumination, the catalyst–dye suspension was stirred in the dark to establish adsorption-desorption equilibrium between the catalyst surface and dye molecules. After reaching equilibrium, the suspension was exposed to the light source, and aliquots were collected at regular time intervals of 30 min. The concentration changes of MB during the reaction were analyzed using a pseudo-first-order kinetic model[6], expressed as $\ln(Ct/C0) = -kt$, where k is the apparent rate constant. As shown in Fig. 7a-b, the kinetic profiles for both samples exhibit two distinct linear regions, indicating that the degradation process proceeds through two stages with different reaction rates. The initial stage is characterized by relatively slow degradation, which can be attributed to the adsorption-desorption equilibrium of dye molecules and the gradual generation of reactive oxygen species on the catalyst surface. In the later stage, the degradation rate increases significantly, suggesting enhanced participation of photogenerated charge carriers and reactive radicals in the oxidation process.

For Zn-doped $NiTiO_3$, the apparent rate constants were determined to be 0.0036 min^{-1} and 0.017 min^{-1} for the first and second kinetic regions, respectively. In contrast, Cu-doped $NiTiO_3$ exhibited substantially higher rate constants of 0.0091 min^{-1} and 0.031 min^{-1} in the corresponding regions. The higher kinetic constants obtained for the Cu-doped sample clearly demonstrate its superior photocatalytic activity. The superior kinetic performance of Cu-doped $NiTiO_3$ is also reflected in the overall degradation efficiency (Fig.7c). After 60 min of visible-light irradiation, Cu-doped $NiTiO_3$ degraded approximately 39% of MB, compared to only

16% for Zn-doped $NiTiO_3$. After 150 min, the degradation efficiency reached 93% for the Cu-doped sample, whereas the Zn-doped sample achieved only 64%. These results confirm that Cu doping is significantly more effective than Zn doping in enhancing the photocatalytic performance of $NiTiO_3$. The contrasting optical and photocatalytic behavior observed in Cu- and Zn-doped $NiTiO_3$ can be understood in terms of their electronic configurations and interactions with the host band structure. When Cu^{2+} ($3d^9$) substitutes at the Ni^{2+} site, its partially filled 3d orbitals introduce localized impurity states within the band gap. These states act as acceptor-like levels and enable additional electronic transitions from the valence band to the conduction band via Cu-derived intermediate states, resulting in an effective narrowing of the optical band gap from 2.1 eV to 1.75 eV and enhanced visible-light absorption. In contrast, Zn^{2+}, with its filled $3d^{10}$ configuration, possesses 3d states that are located deep below the valence band and therefore do not participate in band-edge hybridization. As a result, Zn doping does not introduce mid-gap states or significantly modify the electronic structure, leading to negligible changes in the band gap and optical absorption (Fig. 7d).

Beyond band-gap modulation, Cu doping also plays a crucial role in improving charge carrier dynamics. The presence of Cu^{2+} ions facilitates reversible redox transitions (Cu^{2+}/Cu^{+}), enabling them to act as efficient electron-trapping centers that suppress electron-hole recombination and promote charge separation[63,64]

This improved charge carrier lifetime enhances the generation of reactive oxygen species (ROS), such as superoxide ($O_2\bullet^-$) and hydroxyl (•OH) radicals, which are responsible for the degradation of organic pollutants like methylene blue. In contrast, Zn^{2+} does not provide such charge-trapping functionality due to its closed-shell electronic configuration, resulting in recombination rates and photocatalytic activity similar to those of undoped $NiTiO_3$. Therefore, the superior photocatalytic performance of Cu-doped $NiTiO_3$ arises from the combined effects of band-gap narrowing, enhanced visible-light absorption, and improved charge separation

efficiency, which collectively lead to a higher generation of photogenerated charge carriers under visible-light irradiation.

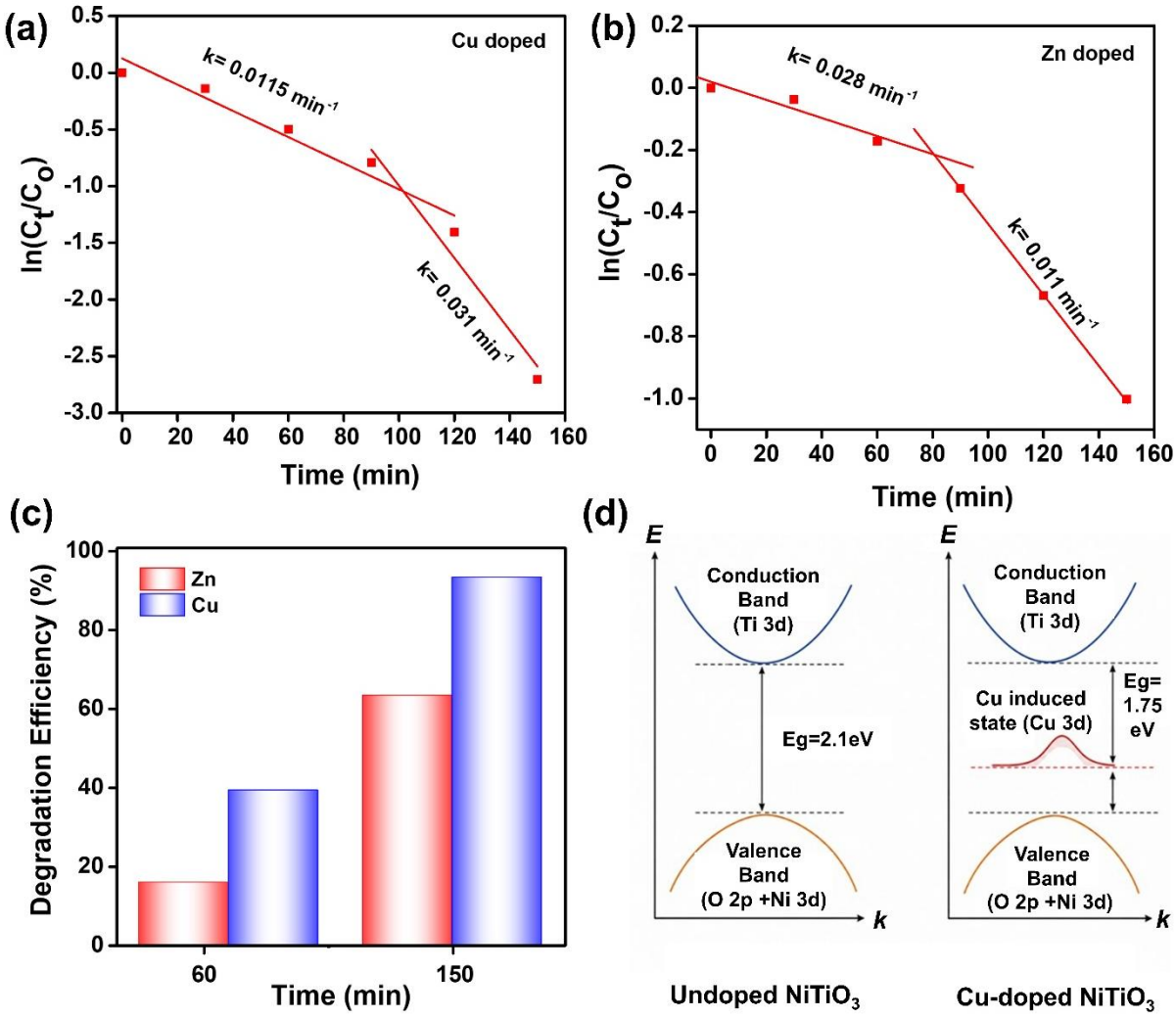


Figure 7. Pseudo-first-order kinetic linear fit for (a) Cu-doped and (b) Zn-doped samples; (c) comparative degradation efficiency at 60 and 150 min; and (d) schematic energy band diagrams comparing undoped and Cu-doped $NiTiO_3$, highlighting the Cu-induced sub-bandgap state.

5. CONCLUSION

In this work, nickel titanate ($NiTiO_3$) nanoparticles were successfully synthesized via a modified Pechini sol-gel route, with controlled incorporation of Cu and Zn dopants at the Ni site. Comprehensive structural and morphological characterizations using XRD, SEM, HR-

TEM, and Raman spectroscopy confirm the formation of phase-pure, nanocrystalline $NiTiO_3$ with well-defined morphology and uniform particle distribution. The introduction of dopant ions induces slight lattice expansion and local structural distortions, while preserving the rhombohedral crystal symmetry and the integrity of the NiO_6/TiO_6 octahedral framework.

Optical investigations reveal that Cu doping significantly modifies the electronic structure, leading to a pronounced redshift in the absorption edge and a systematic reduction of the band gap from ~2.1 eV to ~1.75 eV. This behavior is attributed to the introduction of Cu 3d-derived impurity states and enhanced 3d–2p hybridization near the valence band, which facilitates improved visible-light absorption. In contrast, Zn doping, owing to its fully filled $3d^{10}$ configuration, does not significantly alter the band structure, resulting in negligible changes in optical band gap.

Photocatalytic studies using methylene blue as a model pollutant demonstrate that Cu-doped $NiTiO_3$ exhibits markedly enhanced degradation efficiency under visible-light irradiation compared to Zn-doped and undoped samples. This enhancement arises from the combined effects of band-gap narrowing, improved light harvesting, and efficient charge carrier separation, facilitated by the Cu^{2+}/Cu^{+} redox couple acting as electron-trapping centers. These factors promote the generation of reactive oxygen species responsible for pollutant degradation.

Reference:

[1] K. Nagatsuka, S. Natsume, S. Yoshino, N. Morishita, Y. Yamaguchi, H. Kato, A. Kudo, *J. Phys. Chem. C* **2024**, *128*, 17291.

[2] D. Karmakar, S. Karmakar, A. Ghosh, D. Jana, *Mater. Today Commun.* **2024**, *40*, 110115.

[3] H. Tsubota, A. Jitianu, G. Kawamura, *ACS Mater. Lett.* **2025**, *7*, 1042.

[4] A. C. Mohan, A. Athira, B. P. Nair, G. Sivasubramanian, K. M. Sreekanth, G. Anoop, S. P. Sree, K. M. Sreedhar, *Sci. Rep.* **2024**, *14*, 32067.

[5] P. P. Sarngan, S. Sasi, P. Mukherjee, K. Mitra, Y. Sivalingam, A. Swami, U. K. Ghorai, D. Sarkar, *Nanoscale* **2024**, *16*, 19006.

[6] P. Midya, P. P. Sarngan, A. Dutta, K. Kumar Chattopadhyay, D. Sarkar, *Mater. Sci. Eng. B* **2022**, *286*, 116028.

[7] J. K. Stolarczyk, S. Bhattacharyya, L. Polavarapu, J. Feldmann, *ACS Catal.* **2018**, *8*, 3602.

[8] O. K. Varghese, K. Domen, W. Lipiński, J. Smits, *Appl. Phys. Lett.* **2022**, *121*, 210401.

[9] B. Li, W. Guo, X. F. Lu, Y. Hou, Z. Ding, S. Wang, *Mater. Reports Energy* **2023**, *3*, 100230.

[10] H. Li, H. Gong, X. Hao, G. Wang, Z. Jin, *Renew. Energy* **2022**, *188*, 132.

[11] A. Kudo, Y. Miseki, *Chem. Soc. Rev.* **2009**, *38*, 253.

[12] L. Mu, B. Zeng, X. Tao, Y. Zhao, C. Li, *J. Phys. Chem. Lett.* **2019**, *10*, 1212.

[13] J. Chang, J. He, M. Mao, W. Zhou, Q. Lei, X. Li, D. Li, C.-K. Chua, X. Zhao, *Advanced Material Strategies for Next-Generation Additive Manufacturing*, Vol. 11, **2018**, p. 166.

[14] Y. Xia, C. T. Campbell, B. Roldan Cuenya, M. Mavrikakis, *Chem. Rev.* **2021**, *121*, 563.

[15] K. Szot, M. Pawelczyk, J. Herion, C. Freiburg, J. Albers, R. Waser, J. Hulliger, J.

Kwapulinski, J. Dec, *Appl. Phys. A* **1996**, *62*, 335.

[16] H. Yokokawa, N. Sakai, T. Kawada, M. Dokiya, *Solid State Ionics* **1992**, *52*, 43.

[17] X. Li, H. Zhao, J. Liang, Y. Luo, G. Chen, X. Shi, S. Lu, S. Gao, J. Hu, Q. Liu, X. Sun, *J. Mater. Chem. A* **2021**, *9*, 6650.

[18] L. Yu, X. Pan, X. Cao, P. Hu, X. Bao, *J. Catal.* **2011**, *282*, 183.

[19] S. Gaddimath, K. B. Chandrakala, A. Lagashetty, S. Dani, C. P. K. Prabhu, Giddaerappa, L. K. Sannegowda, *J. Appl. Electrochem.* **2024**, *54*, 2519.

[20] S. Jaiswal, V. Soni, P. Singh, A. Gupta, *ACS Appl. Energy Mater.* **2024**, *7*, 8814.

[21] C. Xin, Y. Wang, Y. Sui, Y. Wang, X. Wang, K. Zhao, Z. Liu, B. Li, X. Liu, *J. Alloys Compd.* **2014**, *613*, 401.

[22] C. Dai, B. Liu, *Energy Environ. Sci.* **2020**, *13*, 24.

[23] Z. Jiang, H. Sun, T. Wang, B. Wang, W. Wei, H. Li, S. Yuan, T. An, H. Zhao, J. Yu, P. K. Wong, *Energy Environ. Sci.* **2018**, *11*, 2382.

[24] S. R. Pendlebury, X. Wang, F. Le Formal, M. Cornuz, A. Kafizas, S. D. Tilley, M. Grätzel, J. R. Durrant, *J. Am. Chem. Soc.* **2014**, *136*, 9854.

[25] B. L. Abrams, J. P. Wilcoxon, *J. Lumin.* **2009**, *129*, 329.

[26] D. Sarkar, C. K. Ghosh, U. N. Maiti, K. K. Chattopadhyay, *Phys. B Condens. Matter* **2011**, *406*, 1429.

[27] S. C., I. M., W. S. F., *Appl. Phys. A* **2025**, *131*, 942.

[28] J. M. Galbraith, *J. Chem. Educ.* **2007**, *84*, 783.

[29] J. Xue, M. Fujitsuka, T. Majima, *Chem. Commun.* **2021**, *57*, 3532.

[30] L. Zhang, W. Chu, Q. Zheng, A. V Benderskii, O. V Prezhdo, J. Zhao, *J. Phys. Chem. Lett.* **2019**, *10*, 6151.

[31] G. M. Whitesides, P. E. Laibinis, *Langmuir* **1990**, *6*, 87.

[32] Z. Wang, L. Yang, C. Xu, J. Cheng, J. Zhao, Q. Huang, C. Yang, *Green Carbon* **2023**, *1*, 193.

[33] D. Bokov, A. Turki Jalil, S. Chupradit, W. Suksatan, M. Javed Ansari, I. H. Shewael, G. H. Valiev, E. Kianfar, *Adv. Mater. Sci. Eng.* **2021**, *2021*, 5102014.

[34] N. Dong, J. He, T. Li, A. Peralta, M. R. Avei, M. Ma, A. E. Kaifer, *J. Org. Chem.* **2018**, *83*, 5467.

[35] M. Blazsó, *J. Anal. Appl. Pyrolysis* **1997**, *39*, 1.

[36] N. Nolan, Sol-Gel Synthesis and Characterisation of Novel Metal Oxide Nanomaterials for Photocatalytic Applications, **2010**.

[37] J.-P. Chen, W.-S. Lin, *Enzyme Microb. Technol.* **2003**, *32*, 801.

[38] T. F. Baumann, A. E. Gash, J. H. Satcher, (Eds.: Aegerter, M. A.; Leventis, N.; Koebel, M. M.), Springer New York, New York, NY, **2011**, pp. 155–170.

[39] V. G. Kessler, G. A. Seisenbaeva, *J. Sol-Gel Sci. Technol.* **2023**, *107*, 190.

[40] L. L. Hench, J. K. West, *Chem. Rev.* **1990**, *90*, 33.

[41] W. Jiang, Y. Zhu, G. Zhu, Z. Zhang, X. Chen, W. Yao, *J. Mater. Chem. A* **2017**, *5*, 5661.

[42] I. Jahan, J. D. Arellano, Z. Shi, *J. Mater. Chem. C* **2025**, *13*, 23675.

[43] Z. Yang, G. Lu, P. Jiang, R. Cong, T. Yang, *Chem. Mater.* **2025**, *37*, 4789.

[44] D. Sarkar, S. Goswami, P. P. Sarngan, L. D, A. P. T, C. K. Ghosh, K. K. Chattopadhyay, *Surfaces and Interfaces* **2024**, *54*, 105247.

[45] D. Sarkar, C. K. Ghosh, K. K. Chattopadhyay, *Appl. Surf. Sci.* **2017**, *418*, 252.

[46] R. Singh, D. Pal, S. Chattopadhyay, *ACS Omega* **2020**, *5*, 21768.

[47] Z. Zhang, Y. Wang, T. Guo, P. Hu, *The Influence of Defect Engineering on the Electronic Structure of Active Centers on the Catalyst Surface*, Vol. 15, **2025**, p. 651.

[48] M. E. Primer, A. A. Berseneva, A. Ulde, W. Sun, R. W. Smaha, *Inorg. Chem.* **2026**, *65*, 7636.

[49] M. Dong, W. Li, L. Geng, R. Huang, H. Han, *ACS Sustain. Chem. Eng.* **2025**, *13*, 15164.

[50] O. El Gardy, T. El-Achari, L. B. Drissi, O. El Fatni, R. Ahl Laamara, *Eur. Phys. J. B* **2025**, *98*, 75.

[51] S. Karmakar, A. K. Manna, S. Varma, D. Behera, *Mater. Res. Express* **2018**, *5*, 55037.

[52] M. A. Ruiz-Preciado, A. Bulou, M. Makowska-Janusik, A. Gibaud, A. Morales-Acevedo, A. Kassiba, *CrystEngComm* **2016**, *18*, 3229.

[53] L. Martín-Carrón, A. de Andrés, M. J. Martínez-Lope, M. T. Casais, J. A. Alonso, *Phys. Rev. B* **2002**, *66*, 174303.

[54] W. Qi, A. Mattursun, M. Gao, A. Hushur, H. Zhang, *Results Phys.* **2022**, *43*, 106114.

[55] M. A. Ruiz Preciado, A. Kassiba, A. Morales-Acevedo, M. Makowska-Janusik, *RSC Adv.* **2015**, *5*, 17396.

[56] C. Selvakumar, V. T. Geetha, A. Jayanthi, C. Baby Gowri, *J. Opt.* **2025**.

[57] Z. Huang, X. Zeng, K. Li, S. Gao, Q. Wang, J. Lu, *ACS Appl. Mater. Interfaces* **2017**,

9, 41120.

[58] M.-W. Li, J.-P. Yuan, X.-M. Gao, E.-Q. Liang, C.-Y. Wang, *Appl. Phys. A* **2016**, *122*, 725.

[59] M. R. Ahmed, N. AbdelAll, G. A. Khouqeer, A. M. Rayan, *Appl. Phys. A* **2026**, *132*, 265.

[60] P. R. Jubu, O. S. Obaseki, D. I. Ajayi, E. Danladi, K. M. Chahrour, A. Muhammad, S. Landi, T. Igbawua, H. F. Chahul, F. K. Yam, *J. Opt.* **2024**, *53*, 5054.

[61] P. Makuła, M. Pacia, W. Macyk, *J. Phys. Chem. Lett.* **2018**, *9*, 6814.

[62] S. Huang, Y. Xu, Q. Liu, T. Zhou, Y. Zhao, L. Jing, H. Xu, H. Li, *Appl. Catal. B Environ.* **2017**, *218*, 174.

[63] L. Ai, Z. Liu, X. Zhang, L. Wang, D. Jia, N. Guo, M. Zha, C. Tan, *J. Colloid Interface Sci.* **2025**, *692*, 137480.

[64] A.B.Quispe Cohaila, E.J.Sacari, W.O.Lanchipa Ramos,R.M.Tamayo Calderon, J.p.Medina Salas, F.Gamarra Gomez, R. Viswanathan Mangalaraja, S. Rajendran, Energies. **2024**, 17 , 3704.